van der Waals Heterostructures based on Three-Dimensional Topological Insulators

Su Kong Chong and Vikram V. Deshpande*

Department of Physics and Astronomy, University of Utah, Salt Lake City, Utah 84112 USA

*Corresponding author: vdesh@physics.utah.edu; Other author: sukong.chong@utah.edu

Abstract

Three-dimensional (3D) topological insulators (TIs) have generated tremendous research interest over the past decade due to their topologically-protected surface states with linear dispersion and helical spin texture. The topological surface states offer an important platform to realize topological phase transitions, topological magnetoelectric effects and topological superconductivity *via* 3D TI-based heterostructures. In this review, we summarize the key findings of magneto and quantum transport properties in 3D TIs and their related heterostructures with normal insulators, ferromagnets and superconductors. For intrinsic 3D TIs, the experimental evidences of the topological surface states and their coupling effects are reviewed. Whereas for 3D TI related heterostructures, we focus on some important phenomenological magnetotransport activities and provide explanations for the proximity-induced topological and quantum effects.

1. Overview

Topological invariants and quantum Hall effects (QHE) are the benchmarks in condensed matter physics which relate the fundamental topological order to quantum mechanical phenomenon in matter. Both concepts apply to an important class of quantum materials, known as topological insulators (TIs). The former is related to the bulk state of the TIs due to a bandgap inversion, while the latter characterizes the topological boundary states due to their nontrivial Berry's phase and Chern number. Because of the topological and symmetry protection, the topological states behave very differently from the ordinary (non-topological) insulator. Such topologically-protected states appear as topological surface (edge) states in three (two) dimensions. A striking property arises from the surface (edge) band crossing at a singularity (known as Dirac point) with a linear dispersion surface (edge) band structure, which can host massless Dirac fermions with unique spin texture [1-4]. The discovery of these topological surface (edge) states has fascinated by their topological related quantum states, such as quantum spin Hall [5] and quantum anomalous Hall [6] effects, arising from the inverted surface gap states with non-trivial topology. These topological effects serve as fundamental grounds for realization of topological phase transitions [7, 8] and more complicated interacting states [9]. Moreover, the topological phases' properties have stimulated research ideas and proposals to realize the unconventional magnetoelectric and quantum phenomena using the heterostructure platforms in TIs.

In this review, we discuss the progress of magneto and quantum transport findings in 3D TIs and their related heterostructures. We begin with the discussion on band inversion induced topology as the origin of the topological surface states (TSS). Depending on the proximitized materials at the termination surface of the 3D TIs, the symmetry protection in the surface states can either be preserved or broken, which can give rise to distinct properties in transport. This thereby signifies the importance of the assembly of 3D TI based heterostructures in a clean manner, where the stacking of atomically flat 2D layered materials is favorable. In the experimental part, we summarize the growth techniques for achieving high quality 3D TIs thin film and their heterostructures. This is followed by the reviews of the magnetotransport signatures, including the Berry's phase from quantum oscillation, half-integer QHE, and surface Landau level (LL) energies in quantum capacitance, to confirm the existence of the TSS. More strikingly, the surface gap induced by intersurface hybridization, magnetic exchange interaction, and superconductivity pairing can lead to intriguing quantum phenomena, including topological phase transitions, unusual electromagnetic activity, and topological superconductivity, etc. in the 3D TI based heterostructures. The important transport results in the different topological surface gapped states are subsequently discussed in the later sections.

1.1 *Band Inversion*

Topologically-protected surface states are a manifestation of their topological invariants in TIs. The topological invariants arise from a concept of band inversion, where the conduction and valence bands are inverted at the bandgap [10]. This band inversion can change the topology of the system to a nonzero quantum number and gives rise to a gapless state at the boundary. This is because the nontrivial topology is a discrete characteristic of inverted gap states, and the topology cannot change as long as the inverted bulk gap remains open. Thus, for the topology to change across the boundary into a trivial one, the gap must close at the interface. This bulk-boundary correspondence guarantees gapless boundary states. Therefore, the band inversion mechanism is also called a topological phase transition.

An important ingredient for the band inversion is spin-orbit coupling (SOC) [10, 11]. SOC arises from the interaction between spin (of electrons) and its orbital motion (of the nucleus) as explained by a general form of Hamiltonian [4] as $H_{SOC}=\lambda\mathbf{L}\cdot\mathbf{S}$, where λ is the SOC strength and $\mathbf{L}$ and $\mathbf{S}$ are the orbital and spin angular momentum operators, respectively. It is known that spin-orbit interaction is a relativistic effect that can cause a distortion in electronic band structures. For a small bandgap element (or compound made of elements) with large SOC, the coupling strength is strong enough to flip the band structure at the gap, causing a negative gap. When this mechanism is associating with a transformation in topological order, topologically protected boundary states can exist. An example of SOC driven band inversion is the CdTe/HgTe quantum well, which is known as the first discovered 2D TI [12]. The prediction was made theoretically [11] based on the inverted band structure of HgTe with zero bandgap at the Γ point due to the strong SOC. The gap is opened by constructing a quantum well with CdTe to break the cubic symmetry. Importantly, although the SOC can shift the band structures, it does not break the existing time-reversal symmetry (TRS) [13].

1.2 *Linear Dispersion Relation*

A consequence of the bulk band inversion with nonzero topology is a pair of boundary states cross at the time-reversal invariant momentum (TRIM). The energy dispersion near this crossing point displays a linear energy-momentum relationship. This dispersion relation is also known as Dirac dispersion as it can be described by the Dirac energy equation in the massless limit [14]. In 2D TIs, it appears as helical edge states, whereas in 3D TIs as surface Dirac cone. This makes TIs the second realized Dirac materials after graphene. Therefore, the surface electrons in 3D TIs are described to behave as massless Dirac fermions. A prominent property of the surface Dirac fermions is that they carry a nonzero Berry's phase [15, 16]. The surface Dirac fermions acquire a π Berry's phase after completing a closed trajectory adiabatically around the Fermi surface. The π Berry's phase has a significant effect on magnetoelectric and quantum transport of the 3D TIs. In magnetoelectric transport, the π Berry's phase causes the Dirac fermions to interfere destructively along the time-reversed scattering paths, leading to the weak antilocalization effect in TSS [17, 18]. This can happen because the TSS conduction channel lies in the quantum diffusion regime where the phase-coherent length exceeds the charges' mean free path, and thus the Dirac fermions maintain their phase coherence upon scattering. In QH regime, the π Berry's phase leads to the half-integer LL filling factor (ν) in Dirac TSS [19, 20], which is distinguishable from the bulk states' LLs.

1.3 *Helical Spin States*

The helical spin polarization in TSS, which is also known as spin-momentum locking, is distinct from the ordinary surface states. The spin in the surface is always pointing to the direction perpendicular to the momentum vector and flipped with opposite momentum. The spin species exhibit a left-handed helicity above the Dirac point and flip to right-handed below the Dirac point [21]. Also, the spin degeneracy in TSS Dirac fermions is lifted because the spin polarization is locked to momentum. This makes the TSS very different from the well-studied Dirac material, graphene, as the latter has both spin and valley degeneracies. Therefore, 3D TI is also ascribed as 1/4 graphene, which offers a simpler platform to study Dirac physics. The spin-momentum locking induced helical spin states naturally gives rise to various interesting spin-related physics. One of the emerging research is the searching of Majorana fermions on TSS in the presence of proximity-induced or bulk doping superconductivity [22, 23]. Another field is 3D TIs based spintronics on generation and detection of the surface spin-polarized current in 3D TI/ferromagnet structure [24].

2. Symmetry Protection and Breaking

2.1 *Gapless Topological Surface States*

The TSS with Dirac energy dispersion and helical spin state can be expressed in a simplified (in the limit of $k \to 0$) 2D effective Hamiltonian as: [25-27]: $H = v(\vec{k} \times \vec{\sigma}) \cdot \hat{n} = v(\sigma_x k_y - \sigma_y k_x)$, where v is the effective velocity, and k and σ denote the wave vector and Pauli matrices, respectively. This linear k term in the effective Hamiltonian infers the linear dispersion of the TSS. The helical spin texture takes the opposite direction for the conduction and valence band. This spin texture is similar to the Fermi surface of 2D electron gas with Rashba SOC, inferring the inversion symmetry is broken at the surface states. These` gapless surface states necessarily emerge when the insulator is physically terminated by an ordinary insulator (including vacuum), as shown in Figure 2a. These gapless surface states are protected by a series of topological protections [21]. The fundamental Z_2 topological invariants guarantee the existence of gapless surface states so long as the bulk gap stays open and inverted. As the spin eigenvalues at opposite momentum states (k and -k) are exactly opposite, electrons with k state cannot be backscattered into the -k state or vice versa because of the spin mismatch [2]. Therefore, the TSS is protected from backscattering. Also, the linear dispersive TSS can host massless Dirac fermions with π Berry's phase, which prevents weak localization through destructive interference paths [28]. The surface states have the remarkable property that they cannot be localized by disorder so long as the symmetries of charge conservation and time reversal are retained.

2.2 *Proximity-Induced Magnetism*

The TSS is protected from nonmagnetic perturbations by TRS, while magnetism is essential to break the TRS. When a 3D TI comes into contact with a ferromagnetic layer (or is chemically doped with magnetic atoms), the spontaneous magnetization induces an exchange field (or exchange coupling), which modifies the electronic structure of the surface states. The effective Hamiltonian by the magnetic exchange coupling can be described as [29, 30] $H_m = m\sigma_z$, where m is the mass term signifies a mass gap proportional to $J_{eff}M$, where J_{eff} and M are the effective exchange coupling and magnetization on the ferromagnetic layer (or magnetic atoms), respectively. The exchange interaction due to the presence of magnetic ordering opens a magnetic gap at the Dirac point (Figure 2b) in the energy spectrum of the TSS and causes the surface Dirac fermions to become massive. The magnetic gap size is proportional to the magnetization and the exchange field strength from the magnetic layer, as shown by the resulting energy dispersion as [31]: $E = \pm\sqrt{v\hbar k^2 + \left(\frac{1}{2}J_{eff}M_z\right)^2}$. For a ferromagnetic layer with out-of-plane magnetization, the induced exchange gap size is $\frac{1}{2}J_{eff}M_z$. The theoretical calculations estimate the magnetic gap is typically in the range of several to tens of meV [29, 32]. The induced magnetism in TSS by proximity effect can also generate an anomalous Hall effect (AHE) in ρ_{xy}, which can be expressed as [33, 34]: $\rho_{xy} = \rho_H B + \rho_{AH}$, where ρ_H and ρ_{AH} are the Hall and anomalous Hall resistivities, respectively. The magnetic exchange gap can modulate the Berry's phase (γ) as [35]: $\gamma = \pi\left(1 - \frac{J_{eff}M_z}{2E_F}\right)$, where E_F is the Fermi energy measured from the Dirac point. This causes the Berry's phase deviation from π and weakens the associated destructive interference in charge transport, leading to the weak localization (WL) effect. In the quantization regime, the induced magnetic gap causes the N= 0 LL pinning to either top valence or bottom conduction bands, depending on the sign of magnetization [36].

2.3 *Proximity-Induced Superconductivity*

When in proximity to a conventional superconductor, superconductivity can be induced in 3D TI by transferring cooper pairs into the TSS. The superconductor coupling can be expressed in a generic form of pairing Hamiltonian as [37, 38]: $H_\Delta = \sum_k \Delta_s c_k^\dagger c_{-k}^\dagger$ and the Hermitian conjugates, where the Δ_S is the superconducting pair potential applying to the electron creation sites in the momentum space. The superconductivity can break the charge conversation symmetry in the surface states without destroying the TRS. As a result of symmetry breaking, a pairing gap can open at the Fermi level due to the proximity effect from the coupling with the superconductor, as illustrated in Figure 2c. This can happen because, in 3D TIs, the dispersion relation of the opposite spin states is an even function of momentum k due to the TRS. The induced pairing gap can transform the energy spectrum at the Fermi level of the 3D TI to $E = \pm\sqrt{v\hbar k^2 + \Delta_s^2} - E_F$ [39]. The pairing gap is generally smaller than the superconducting gap of the contacted superconductor, where Δ_S^2/E_F is typically of the order of μeV [40]. TI/SC heterostructures have generated tremendous interest in the condensed matter community as they can induce an unconventional superconductor in 3D TIs, called a topological superconductor, with topological vortices that can host Majorana bound states [22, 41-43]. The existence of Majorana quasiparticle states have been suggested by a variety of experiments in transport and spectroscopies in the detection of Majorana zero modes [44, 45], Majorana bound states [46-48], and chiral Majorana edge states [49].

3. Materials Growth

The striking TSS characteristic has stimulated tremendous interest over the past decade to search for the ideal candidates. To this end, the Bi_2Se_3 family with a relatively large bulk gap ~300 meV and simple Dirac cone surface state has stood out from the competition [3, 4, 50]. Nevertheless, as the gap size is equivalent to a small gap semiconductor, significant bulk conduction was observed in Bi_2Se_3 due to its natural doping as inferred by its metallic temperature dependency. The early research on 3D TI devices has been focused on the isolation of surface transport from the bulk and the elimination of bulk carriers for the convenience of probing their surface states. Tremendous efforts have been made in materials synthesis to achieve the truly bulk insulating 3D TIs with high surface mobility.

Various growth methods have been experimented with by material science growers to produce high-quality 3D TI single crystals. The synthesis methods can generally be grouped into three types according to their outcomes, namely nanostructures, thin films, and bulk crystals, as illustrated in Figure 3. A convenient method to grow crystalline nanostructures, such as 2D nanoflakes, nanoribbons, and 1D nanowires, etc. is chemical vapor transport (CVT). In CVT, the vapor precursors (vapors or vaporized solids) react through thermal reactions, transport by carrier vapor, and condense on a solid substrate. CVT is extremely advantageous in preparing low dimensional nanowires for probing 1D physics, such as Aharonov Bohm oscillations [51-53] and Coulomb blockade [54]. Nevertheless, the CVT-grown 2D flakes are usually small (hundreds of nanometers to microns) [55] and thus device fabrication is challenging. In contrast, molecular beam epitaxy (MBE) is known to produce a thin film with a large area of epitaxial growth [56] and controllable thickness. Another benefit of the MBE system in growing 3D TIs is controllable doping. For example, tuning the chemical composition ratio between Bi and Sb can eventually lead to the intrinsic $(Bi,Sb)_2Te_3$ 3D TI [57]. However, the only disadvantage of MBE is its stringent substrate-dependent which requires lattice matching to the growth materials. Another widely used method is the preparation of high mobility 3D TI is the random exfoliation from the bulk crystals. Similar to graphene, the Bi_2Se_3 family 3D TIs are layered materials with van der Waals bonding between each quintuple layer, which can be exfoliated into thin flakes using the scotch tape method. This method has also been used intensively to prepare heterostructures with other 2D or bulk materials by stacking method using a micromanipulator. The advancement in random exfoliation and dry transfer techniques in van der Waals layered materials has opened a new opportunity for high quality electronic devices with clean interface [58-60]. As the device quality strongly depends on the quality of the parent crystals, the bulk crystals growers play an important role to optimize the growth conditions for single crystals with desired stoichiometry and crystallography phase. Typically, high-quality 3D TI bulk crystals were grown by vertical Bridgman or flux methods [19, 61, 62].

Table 1 Summary of the utilities and drawbacks of the different growth methods for 3D TIs

Method	Utility	Drawback
Chemical vapor transport	• 1D nanostructures for 1D physics • 2D nanocrystals	• Limitation of sample size (submicron to microns) • Limit to mesoscopic-scale device
Molecular beam epitaxy	• Large area epitaxial growth • Thin film with controllable thickness • Heterostructures with clean interface	• Require lattice-matching to the substrate
Melt-growth/ Flux-growth/ Bridgman-growth	• Large grain size/single-crystal • High mobility • Allows van der Waals stacking with other 2D materials	• Challenging exfoliation for thin flakes with uniform thickness

4. Evidence of Topological Surface States

4.1 *Ambipolar Conduction*

Although the 3D TI with the topologically protected surface state had been discovered in photoemission spectroscopy almost instantly after the prediction, it has taken much longer for transport experiments to demonstrate the most fundamental signature of surface states, namely the ambipolar Dirac electronic transport and their unique Landau quantization. A key challenge holding up the progress is the significant bulk carriers, which impede the surface conduction. For example, in Bi_2Se_3 3D TI, the single Dirac cone surface state guarantees an ambipolar electron-hole transport with a gapless Dirac point. However, the heavy n-type doping in Bi_2Se_3 due to Se vacancies shifts the Fermi level deep into the bulk conduction band, which limits the access to its surface band. Progress towards this end has been made to reduce the bulk carrier density by extrinsic chemical doping in the thin sample. Ambipolar field effect with minimum conductivity at charge neutrality point was reported by Kim et al. [63] in Bi_2Se_3 thin flake by applying electrolyte top gating together with Si/SiO_2 bottom gate control (Figure 4a, top panel). The chemical doping with F4TCNQ electrolyte was applied to induce p-type doping to the bulk. The weak temperature-dependent $\rho_{xx}(V_g)$ peak was assigned to its gapless Dirac point, similar to graphene. The ambipolar behavior with hole and electron carriers were confirmed from its Hall carrier density, n_H, plotted as a function of gate voltage. As shown in Figure 4a (bottom panel), the n_H shows a sign change at the $\rho_{xx}(V_g)$ peak and the hole (electron) density increase linearly with increasing V_g to both ends. These results verified the ambipolar transport is originated from the surface state rather than from the bulk band.

4.2 *Quantum Oscillations*

A prominent property of surface Dirac fermions is the Landau quantization of their energy states in the presence of a perpendicular magnetic field. A classical picture of the Landau quantization can be viewed as the surface Dirac fermions confined in the cyclotron orbits with finite energy states known as LLs. When a 3D TI is subjected to a magnetic field, the density of states (DoS) is periodically modulated as a function of magnetic field due to the change of DoS across different LLs. This leads to an oscillating feature in longitudinal resistivity (or conductivity) known as Shubnikov–de Haas (SdH) oscillations. The SdH oscillations provide an effective way to quantitatively characterize the TSS even if it overlaps with the 3D bulk states. In SdH oscillations regime, the longitudinal conductivity (σ_{xx}) follows the relation [64]: $\Delta\sigma_{xx} = \sigma_{xx}^{0} \cos\left[2\pi\left(\frac{B_F}{B} - \frac{1}{2} + \beta\right)\right]$, where B is the external magnetic field, B_F is the oscillation frequency, and β is the phase factor ($0 = \beta < 1$). The parameter β is related to the Berry's phase γ by a factor of 2π. The Berry's phase is zero for a parabolic energy dispersion (β= 0) and, as already noted, π for Dirac fermions with linear energy dispersion (β= 1/2). For bulk conducting 3D TIs, the phase factor directly reflects the Berry's phase of the system, which can be used to distinguish the Landau quantization from the 2D electron gas from the bulk states and Dirac fermions from the TSS. The phase factor β in the SdH oscillations can be experimentally determined from an analysis of the LL fan diagram, in which the N^{th} minima in σ_{xx} are plotted against their corresponding reciprocal values of a magnetic field ($1/B_N$). From the $\Delta\sigma_{xx}$ relation, the N^{th} minima occur when the argument of the cosine term equals (2N-1)π, which simplifies the relation to $N = \frac{B_F}{B_N} + \beta$. Therefore, the plot of N *versus* $1/B_N$ makes a straight line with a slope of B_F corresponding to the oscillation frequency. The linear fit to the LL fan diagram can be extrapolated to zero limits of $1/B_N$, and the intercept on the N-index axis gives the phase factor β. Depending on the β value obtained from the fan diagram, one can conclude the origin of the conduction channels to the SdH.

Quantum oscillations arisen from the TSS were reported by Qu et al. [65] in Bi_2Te_3 bulk crystal. Figure 4b shows the SdH oscillations correspond to successive occupying of LL as the magnetic field is increased. The surface origin of the SdH oscillations was confirmed by analyzing the angular dependence of the oscillation frequency. For non-metallic (light bulk doping) samples, the LL minima as a function of tilt angle θ coincide well with 1/cosθ curve, in contrast to the deviation for their metallic (heavy bulk doping) samples. The derived surface mobility >9000 cm^2/Vs is 10 times greater than bulk carrier mobility. Nevertheless, the 2D surface states only account for ~0.3% of the total conductance at 0.3 K, which indicates a significant bulk carrier conduction in Bi_2Te_3 3D TIs. This limits the access of Landau quantization near their surface states Dirac points. Later, the successful growth of quaternary tetradymite $Bi_{1.5}Sb_{0.5}Te_{1.7}Se_{1.3}$ crystals was found to achieve a large surface contribution up to 70% [66]. Cleaner SdH oscillations were observed in $\rho_{xx}(B)$ curve for the 30 µm-thick $Bi_{1.5}Sb_{0.5}Te_{1.7}Se_{1.3}$ crystal. Interestingly, the carrier type of the $Bi_{1.5}Sb_{0.5}Te_{1.7}Se_{1.3}$ crystal changes from a hole in fresh to electron-doped in aged conditions, as indicated by the sign change in Hall coefficient. The constructed LL fan diagram (Figure 4c) from surface states across the Dirac point presents a non-zero (close to 0.5) intercept β, reflecting the non-ideal π Berry's phase in the TSS presumably due to the conducting bulk channel. Moreover, the fittings to the LL fan to Dirac model give the band parameters: Fermi velocity, $v_F = 4.6\times10^5$ m/s, effective mass, $m^* = 0.32m_e$, and surface g-factor, $g_s = 20$, which shows a good agreement with the photoemission spectroscopy.

4.3 *Half-Integer Quantum Hall Effect*

In a strictly 2D electron system, SdH oscillations occur as a precursor of the QHE. Similar to SdH oscillations, QHE is a manifestation of LLs for the Dirac fermions confined in 2D surface states. The difference is that SdH oscillations typically detect the large N^{th} LLs, whereas QHE probes the lower indices LLs due to the larger energy spacings. QHE is a quantized version of the Hall effect, which can be probed by measuring the transverse charge flows in a perpendicular magnetic field. The 2D conductivity tensor is derived from the inverse of the resistivity tensor as: $\begin{pmatrix}\sigma_{xx} & \sigma_{xy}\\ \sigma_{yx} & \sigma_{xx}\end{pmatrix} = \begin{pmatrix}\rho_{xx} & \rho_{xy}\\ \rho_{yx} & \rho_{xx}\end{pmatrix}^{-1} = \frac{1}{\rho_{xx}^2+\rho_{xy}^2}\begin{pmatrix}\rho_{xx} & \rho_{xy}\\ \rho_{yx} & \rho_{xx}\end{pmatrix}$, where σ_{xy} and ρ_{xy} are the Hall conductivity and resistivity. In the QH regime, when the Fermi level is controlled in between two neighboring LLs, the σ_{xx} reduces to a minimum as the DoS vanishes inside the LL gap, while the σ_{xy} develops into a Hall plateau, which quantizes at an integer factor of e^2/h. When the Fermi level is inside an LL, the σ_{xx} takes a finite value, and the σ_{xy} changes toward the next filling level. QHE in surface states of 3D TIs exhibits several unique behaviors owing to their π Berry's phase and zero spin degeneracy. The π Berry's phase has an important impact on the surface quantization. The LL filling factor (ν) for Dirac fermions is not proportional to the LL index (N) but follows a proportionality of $\nu = g\left(N + \frac{1}{2}\right)$, where the degeneracy g= 1 for the non-degenerate spin species. This infers the half-integer QHE in Dirac TSS. While the early works showed ambipolar transport or quantum oscillations in 3D TIs, these are not smoking gun signatures of the topological surface states as these signatures can also appear in semiconductors with normal band gap or trivial surface states. However, the π Berry's phase and half-integer QHE discussed in this section mark solid evidences to distinguish topological surface states from trivial band insulators.

The success in suppression of bulk conduction in ternary and quaternary Bi-based tetradymite has stimulated the surface QHE at a strong magnetic field as reported by Yoshimi et al. [20] in

$(Bi_{1-x}Sb_x)_2Te_3$, and Xu et al. [19] in $BiSbTeSe_2$ 3D TIs. Although the ν takes a half-integer value in the surface QHE, the individual half-integer QH conductance of each surface cannot be measured directly in a standard Hall measurement. The top and bottom surface states with two independent Dirac fermions form a pair of edge mode conducting channels at the surfaces in a perpendicular magnetic field. Thus, the fully quantized Hall plateaus at integer number are attributed to the consequence of two states of half-integer QHE from the top and bottom surface states, and the σ_{xy} can be expressed as [19, 20, 61]: $\sigma_{xy} = (\nu_b + \nu_t)\frac{e^2}{h} = \left[\left(N_b + \frac{1}{2}\right) + \left(N_t + \frac{1}{2}\right)\right]\frac{e^2}{h}$, where the N_t and N_b are the LL indices of top and bottom TSS, respectively. The ν_t or ν_b change sign when crossing the $N_t = 0$ or $N_b = 0$ LLs. As shown in Figure 4d, the TSS QH plateaus always take integer steps as a result of the fixed top surface LL filling factor of 1/2 while the bottom surface LL filling changed by Nb+1/2 with the backgate voltage. Follow-up work by Xu et al. [67] resolves a series of integer QH states corresponding to top and bottom surface LLs as controlled by the top and bottom gates. Figure 4e shows the color plots divide the dualgate axes into a series of QH parallelograms, centered around well-developed or developing QH states with quantized σ_{xy} in integer units of e^2/h. The $N_{t(b)}$ is the corresponding top (bottom) surface LL integer index that can be adjusted by the top (back) gate to be of either Dirac electrons or holes.

An interesting quantum state in 3D TIs is the $\nu = 0$ QH state, which emerges as the top and bottom surfaces fill the LLs with the opposite sign filling factors, $\nu_t = -\nu_b$. As shown in Figure 4e, A diagonal series of $\nu = 0$ Hall plateaus (white regions) separate the electron-dominated regions in red and the hole-dominated regions in blue. This implies that the $\nu = 0$ QH states in 3D TIs is a resultant of their counterpropagating edge channels. Unlike the other integer QH states in TSS that carry dissipationless edge modes, the $\nu = 0$ state is dissipative; namely, the ρ_{xx} tends toward maximization (instead of vanishing) in the magnetic field. Following the conductivity tensor calculation, both the σ_{xy} and σ_{xx} tend to develop towards zero when $\rho_{xx} >> \rho_{xy}$. The disorder can cause scattering between the counterpropagating states, resulting in the non-chiral dissipative transport with large resistance.

4.4 *Surface Landau Level Energies*

The TSS LLs follow a Dirac LL energy relation as [68, 69]: $E_N = sgn(N) v_F \sqrt{2e\hbar|N|B}$, where N is the LL index, and v_F is Fermi velocity. The surface LL energy spacing changes as a square root of N, as opposed to constant energy spacing in ordinary metals and insulators. Also, different from the linear proportionality with the magnetic field in an ordinary insulator, the TSS's LL spacing scales as a function of the square root of magnetic field. Another important signature is the N= 0 LL, which is pinned to the Dirac point of the TSS and independent of the magnetic field. This generates an LL fan with a symmetrical appearance of the square root of N states on both the positive (electron) and negative (hole) energy sides of the Dirac point. Besides that, it is important to note that the LL energy is indexed to N instead of ν, meaning that the LL energy relation is applied to individual surface LLs. Experimentally, it is highly favorable to study the TSS LLs in energy parameter space. The surface LL energy in $BiSbTeSe_2$ was estimated from the thermal activation energy of ~6 meV at 31 T [19], which is much smaller than the theoretical value (~60 meV), presumably due to the thermal smearing. Alternatively, quantum capacitance (C_Q) is directly related to the density of states, which allows a quantitative evaluation of the surface LL energies in 3D TI. The C_Q forms dip at a minimum DoS corresponding to a gap feature. The C_Q can be expressed as [70-73]: $C_Q = Ae^2\frac{dn}{d\mu}$, where A, n, and μ are the effective surface area, surface charge density, and chemical potential, respectively. The chemical potential-density relation, $\mu(n)$ can thus be obtained by integrating the electronic compressibility ($d\mu/dn$) with respect to n.

Figure 5a shows the color map of the chemical potential (μ_b) as a function of charge density (n_b) of the bottom surface of a $BiSbTeSe_2$ thin flake (~17 nm) measured at different charge density (n_t) of the top surface [74]. The $\mu_b(n_b)$ curves taken at the four different QH states near the center CNP with (ν_t, ν_b) of (-½,-½), (-½,+½), (+½,-½) and (+½,+½) are shown in Figure 5b. The step height in μ_b indicates the LL spacing Δ_b of the corresponding QH state. The Δ_b of ~40±2 meV at the magnetic field of 18T agrees well with the Dirac LL energy relation for TSS. Interestingly, the comparable energy spacing for the ν= 0 and ±1 QH states inevitably confirms that they all lie in the lowest LL gap i.e. $\Delta_{0,-1}$ and $\Delta_{+1,0}$. The top and bottom TSS can be individually probed by applying excitation voltages to the gates coupled capacitively to different surfaces. As a result, the LL energies of each surface state can be extracted. Figure 5c summarizes the top and bottom surface LL energies, E_b and E_t for the ν= 0 and ±1 QH states. In ν= +1 (-1) QH states, the E_b and E_t display the same sign for both N_b and N_t because the chemical potentials of both surfaces reside in electron (hole) LLs. This is consistent with the origin of parallel-propagating states in conduction. Whereas the E_b and E_t reveal the nearly equal magnitude and opposite sign for the two ν= 0 QH states due to the opposite occupation of at N_b and N_t. The LL energies from the top and bottom surfaces balance out and give rise to the ν= 0 states.

4.5 *Surfaces' Capacitive Coupling*

When the thickness of the 3D TIs is comparable to the magnetic length, $l_B = \sqrt{\frac{\hbar}{eB}}$ [75], the top and bottom surfaces become strongly correlated because of the intersurface interaction under application of a strong magnetic field. The correlated topological excitonic gapped state is a quantum coherent gapped state involving only the interlayer Coulomb interaction [76, 77]. When the top and bottom surfaces are independently doped to induce electrons in one layer and holes in the other, the interlayer electron-hole pairs form indirect excitons, which can support the topological exciton condensate at low enough temperature. This correlated state can occur when a 3D TI film is thinned to a thickness where the top and bottom surface states are coupled strongly yet not strong enough for their wave functions to hybridize. This usually appears at 2D surface separations in an order of l_B. The relatively flat LL band serves as a ground for the topological excitonic condensate, while the lowest QH state with the widest separation from other LLs is ideal for the realization of this effect.

On the other hand, for thin enough 3D TIs, applying a gate voltage on one surface affects the charge density in the other through a capacitive coupling effect, which may interplay with the topological excitonic state in the thin limit. Our work [78] on thickness-dependent QHE of $BiSbTeSe_2$ 3D TI shows the capacitive coupling effect can also affect the gate-dependent QH transitions under magnetic field of 18T, which may enable insight into this phenomena. The intersurface capacitive coupling effect is revealed by the bending of the QH plateau-to-plateau transition, as traced by the dashed lines in the dualgate map (Figure 5d), where screening in the bulk is weaker at the low carrier density region. This leads to a pronounced bending of N_t= 0 and N_b= 0 tracelines near the overall CNP as observed in thinner samples. From the fitting to the charge density of the top surface modulated by the bottom gate, a thickness-dependent capacitive coupling effect can be illustrated by the color scale bar, where blue and yellow represent the capacitively-coupled and decoupled surface states, respectively. As a consequence of the capacitive coupling, a zeroth LLs anti-crossing causes the splitting in both N_t and N_b= 0 LLs at the overall CNP. The resulting zeroth QH plateau formed at the CNP is attributed to a gap opened at the Dirac point. The origin of this gapped state can be ascribed to the hybridization between the top and bottom surface states. A key signature of the intersurface hybridization is the degeneracy lifting of the N= 0 levels in Landau quantization [79-82]. Note that, as the gap feature is observed at a thickness above the 2D limit (< 10 nm) and a reasonably high magnetic field, there is a possibility of the excitonic insulator gap [83] developed in this regime. Moreover, the width of the zeroth Hall plateau at the CNP increases slowly from 16 down to 10 nm as oppose to the exponentially increment expected in the hybridization gap, suggesting the existence of a weak thickness-dependent gapped state other than the single-particle tunneling gap.

5. Topological Phase Transitions

5.1 *Finite Size Effect*

Each surface state in a 3D TI is associated with its own Dirac cone wavefunction. The TSS breaks down at a finite film thickness when the wavefunctions between the top and bottom surface states overlap. The intersurface hybridization leads to a mass gap open at the Dirac point and thus is called the hybridization gap. The Hamiltonian of the TSS is modified by the finite mass term in the effective 2D model as: $H_p = \Delta_h \sigma_z$, where the Δ_h represents the hybridization matrix element. The hybridization gap size scales up exponentially with a decrease in layer number of 3D TI due to the strong tunneling between the surfaces [79-82, 84]. Figure 6a illustrates the hybridization of top and bottom surface bands to form the hybridization gap in the surface spectrum as the film thickness reduces below d_c. Here the d_c is defined as the thickness above which there is no measurable surface gap. Similarly, the hybridization gap can result in a decline in the π Berry's phase of the TSS, where the modified Berry's phase is related to the hybridization gap as [85]: $\gamma = \pi\left(1 - \frac{\Delta_h}{E_F}\right)$. This causes the Berry's phase to deviate from π and weakens the associated destructive interference in charge transport. A direct consequence of the reduced Berry's phase is the constructive quantum interference in the electronic paths of massive Dirac fermions, leading to the weak localization (WL) effect. The competition between WL and the preexisting WAL lead to an opposite trend in $\Delta\sigma_{xx}$ with magnetic field in magneto-transport [86, 87]. Also, the hybridization gap opening at the Dirac point can lead to a decline of the metallic surface transport. The hybridization gap can be more reliably shown in temperature dependence transport in ultrathin 3D TIs. As shown in Figure 6b, the resistance of Bi_2Se_3 films systematically change with thickness from bulk down to 2 quintuple layers (QL) [88]. The metallic behavior was observed in thick films, while a sharp divergence at low temperature was observed as the thickness reduced below 5 QL. This insulating behavior is strong evidence of the insulating ground gapped state due to the intersurface hybridization. The hybridization gap size can be calculated from the thermal activation energy as demonstrated by Cho et al. [89] in a 3 QL Bi_2Se_3 flake with a 250 meV surface energy gap.

5.2 In-Plane Magnetic Field Effect

For TSS with a small hybridization gap, the gapped surface band structure evolves under a magnetic field applied in-plane to the 3D TI film surface. Different from the perpendicular magnetic field which increases the surface bands splitting and causes a nearly linear increment of the hybridization gap with the magnetic field [81], the film undergoes a quantum phase transition from an insulating to a semimetallic state, driven by the parallel magnetic field. This magnetic field-driven topological phase transition was proposed by Zyuzin et al. [90] in hybridized 3D TIs. A magnetic energy is defined in their model as $\varepsilon_B = v_F \kappa_B$, where $\kappa_B \sim d/2l_B^2$, to explain the surface band shifting. As illustrated in Figure 6c, when the $\Delta_h > \varepsilon_B$, the band structure consists of a pair of quadratic bands corresponding to the top and bottom hybridized surface bands, split by the TRS-breaking gap at $k = 0$. As the magnetic field increases, the two quadratic bands shift oppositely along the vertical axis (Zeeman-like band splitting). At $\Delta_h = \varepsilon_B$, the quadratic band closes at the conduction and valence band edges and turns the film into a semimetal. The band dispersion remains quadratic along k_y, but is linear in k_x. Further increasing the magnetic field ($\Delta_h < \varepsilon_B$) will shift the bands to two crossing Dirac points separated in k_y axis by $2\kappa_0 = 2(\varepsilon_B^2 - \Delta_h^2)^{1/2}/\nabla v_f$. Eventually, the film turns into a Dirac semimetal.

The experimental observation was reported by Xu et al. [91] in a ~10 nm thin $BiSbTeSe_2$ where a giant negative MR was observed by applying an in-plane magnetic field. As shown in Figure 6d, the ρ_{max} of the hybridized $BiSbTeSe_2$ drops by a factor of ~20 (giving an MR~-95%) from a resistive value of ~$12h/e^2$ at zero magnetic field to a value ~$0.55h/e^2$ at the magnetic field of 45 T. The corresponding insulator-semimetal transition can be interpreted by the previously discussed theoretical prediction, where the in-plane magnetic field can introduce the opposite Zeeman-like shifting of the top and bottom surface Dirac cones in the momentum space. Also, an effective Zeeman energy was introduced by taking into account the spin and orbital magnetic moments modified g-factor, as $E_B = g_{eff}\mu_B B$. The experimentally obtained gap closing rate, E_B/B of about 0.02 meV/T, which give rise to an in-plane g-factor of ~20.

5.3 Perpendicular Electric Field Effect

An external perpendicular electric field can drive the surface bands and transform between topologically trivial and non-trivial states in a hybridized 3D TI. This is possible because the perpendicular electric field can break the spatial inversion symmetry by applying a potential difference between the top and bottom surfaces, and results in a surface band shifting. A necessary condition for the electric field-induced topological phase transition is a gap-closing point, where the topological invariant exchanges between the topologically trivial ($\nu = 0$) and non-trivial ($\nu = 1$) phases after gap reopening. While the gap closes at points other than the TRIM in such an inversion-asymmetric system [92-94]. As shown in Figure 6e, applying an $E_\perp$ perpendicular to the hybridized 3D TI can cause the upper (lower) surface bands to shift upward (downward) in energy, and the surface band structure shows a Rashba-like band splitting. This results in a reduction in the surface hybridization gap and as it shifts away from the TRIM. The topology of the film does not change until the $E_\perp$ reaches a gap-closing point at E_C. As the $E_\perp$ exceeds E_C, the surface gap reopens with a non-trivial topological invariant ($\nu = 1$), which can host a topological edge state.

Experimentally, the electric field-induced gap closing mechanism was reported by Zhang et al. [95] in Sb_2Te_3 thin film using an STM probe. However, the electric field strength is limited to < 100 mV/nm where only a small range of gap modulation is observed. We demonstrated a prominent electric field response in a 9 nm hybridized $BiSbTeSe_2$ by showing more than an order of magnitude reduction in ρ_{xx} with the applied displacement field (D) via a dualgating [96]. As shown in Figure 6f, the ρ_{xx} (~$13h/e^2$) falls significantly with D and tends to saturate to a value close to the order of $h/2e^2$ at large D > 150 mV/nm, implying a suppression of the hybridization gap at large D. The surface gap sizes at different D are probed by the thermal activation behavior, different conductance and quantum capacitance to provide quantitative analysis on the gap-closing feature. This perpendicular electric field-induced gap-closing in the hybridized $BiSbTeSe_2$ provides a strong indication of the topological phase transition, where the surface hybridization gap transforms from a trivial gap to a 2D topological gap. The saturated ρ_{xx} ~$h/2e^2$ supports the development toward quantum spin Hall edge states at large D.

6. Novel Topological Insulator-based Heterostructures

6.1 *Topological Insulator/Ferromagnet Heterostructures*

The magnetic proximity effect can induce an exchange gap in 3D TIs and gives rise to the anomalous Hall effect. In TI/FM heterostructures, the exchange field strength depends strongly on the interface quality. Note that this kind of heterostructures has been widely studied in spintronic devices, in particular spin-orbit torque switching [24, 97-99]. However, this area is not the focus of this review as it can be found in other review articles [100-102]. Following the realization of QHE in 3D TIs, the magnetic exchange coupling to the surface QH states was demonstrated by the following experiments. A study on Co-clusters-decorated $BiSbTeSe_2$ by Zhang et al. [36] revealed an anomalous quantization trajectory resulting from the magnetic exchange gap. Figure 7a and 7b show the QH states of the Co-clusters-decorated $BiSbTeSe_2$ with a quasi-half-integer $\nu= -3/2$ Hall plateau evolves at a medium field of -7.2 T. Renormalization group flow (RGF) diagram has been used to examine the flow patterns and extract the converging points of the QH states in (σ_{xy}, σ_{xy}) space [103]. In Figure 7a, a flow diagram in σ_{xy} versus σ_{xy} plane (based on the gate-dependent data points) was plotted to analyze the flow between the integer QH states and the intermediate $\nu= -3/2$ state at different magnetic field. The $\nu= -3/2$ QH plateau is attributed to the contribution of one being the $\nu= -1/2$ quantized bottom surface undecorated TSS and the other being the $\nu= -e^2/h$ Hall conductivity from the top surface with Co-decoration. A delayed LLs hybridization model was introduced to explain the anomalous quantization step. Magnetic moments of the Co clusters induce a sizeable Zeeman-like exchange gap in the top surface through an antiferromagnetic coupling. The magnetic exchange gap causes a shift in zeroth LL to the conduction band edge, which leads to an increase in the distance between $N_t= -1$ and 0 LLs. This affects the LL quantization of the $BiSbTeSe_2$ at the moderate magnetic field when the LL energy spacing is comparable to the magnetic exchange gap. As illustrated in Figure 7c, at the lower magnetic field, the $\nu= -1$ LL hybridization of the top decorated surface is delayed by the extended LL spacing due to the exchange gap. As a result, the top and bottom surfaces reach the same LL at the different magnetic fields, leading to the anomaly in the quantization trajectory. An estimation of the LL width yields a lower bound of 4.8 meV for the magnetic exchange gap induced by the Co clusters.

In the vdW platform, our group has explored similar type of devices in the $BiSbTeSe_2/CrGeTe_3$/graphite heterostructures configuration [104]. Different from the Co clusters, the $CrGeTe_3$ (CGT) is a layered ferromagnetic insulator (FMI). An electrostatic gating can be applied through the CGT dielectric layer, which has been prohibited in the Co-clusters layer due to the screening effect. The TSS can also be gapped by the proximity coupling to the CGT. Additionally, the success in applying top gating *via* CGT/Gr gate to tune the chemical potential of the gapped top surface state is revealed by the developed QH states in the dualgate map (Figure 7d). The four-quadrant QH plateaus formed near the overall CNP are highly asymmetric with the $N_t= -1$ and $N_t= 0$ LLs extended over a longer range in topgate voltage than the $N_t=0$ and $N_t=1$. This asymmetry is attributed to the exchange gap opening due to the TRS-broken surface state by the CGT, as illustrated by the surface band structure. The magnetic gap opened at the top surface Dirac point causes an upshift in the $N_t= 0$ LL, residing at the bottom of the conduction band. The magnetic exchange gap size evaluated from the asymmetry in the LL spacing is ~26 meV at 9T. Besides, with the access to the top gapped surface state, an additional quantization plateau of $-e^2/2h$ was observed in $\sigma_{xy}(V_{tg})$ curve in comparison to the normal QHE with integer e^2/h steps in $\sigma_{xy}(V_{bg})$, as shown in Figure 7e. This half-quantized step developed between the $\nu= -1$ and 0 QH states is ascribed to a quasi-zeroth Hall plateau pinned at the transition of the top surface Hall conductivity, σ_{xy}^{t} from $-e^2/2h$ to $+e^2/2h$, with the bottom surface is kept at $\sigma_{xy}^{b} = -e^2/2h$.

The observation of quasi-half-integer QH conductance in both Co-decorated and CGT proximitized $BiSbTeSe_2$ samples can have important consequences in condensed matter and high energy physics. The massive Dirac fermions in magnetic gapped TSS can exhibit a parity anomaly arising from parity symmetry breaking [105-107]. The resolved unconventional half-quantized QH plateau in magnetic-coupled 3D TIs provides a platform to realize the parity anomaly. On the other hand, the quantization in TI/FMI heterostructures is favorable for the study of the topological magnetoelectric effect (TME), as proposed by Qi et al. [108] and Wang et al. [109] in an FMI encapsulated 3D TI configuration. The FMIs in this configuration play two important roles, namely the induction of the magnetic exchange gap and chiral edge states on the TSS. A general description of the TME is an electric (magnetic) field that generates a topological contribution to an antiparallel magnetization (electric polarization) with a universal constant of quantization in units of e^2/h. This exotic electromagnetic response in 3D TIs can be described by a modified Lagrangian (L_{TI}) that includes an axion $E \cdot B$ and a dimensionless topological θ terms in addition to the conventional Maxwell term [108-110]: $L_{TI} = \frac{e^2}{2h}\frac{\theta}{\pi} E \cdot B$, where under time-reversal invariant, the topological θ term is equal to π (modulo 2π) for TI and zero in a vacuum or ordinary insulator.

6.2 *Topological Insulator/Superconductor Heterojunctions*

Superconductivity in 3D TIs is of great interest as it provides a promising route to realize a nontrivial topological superconducting state. The topological superconductivity stems from the Cooper pairing of spin-polarized surface state electrons when proximitized by a conventional s-wave superconductor, and such a "spinless" p_x+ip_y pairing superconductor can host a self-conjugate electron called Majorana fermion [41, 111]. The localized Majorana fermions in vortices of topological superconductors form Majorana zero-modes, which obey non-Abelian statistics and are useful for topological quantum computation [112].

A variety of device schemes have been proposed to probe the Majorana modes in the topological superconductor, including zero-bias conductance, 4π periodic Josephson effect, and half-quantized conductance plateau, etc. At a basic level, these effects rely on the superconductivity in the proximitized 3D TI film, which can be proved by probing the induced pairing gap. Differential conductance has been widely used to measure the superconductor gap spectrum. Depending on the transparency of the superconductive contact, the differential conductance spectrum can vary from a plateau that is almost twice as high as the normal state conductance (for perfect transparency) to a dip with zero conductance due to the high barrier interface (for poor transparency) [113, 114]. While the width of the differential conductance plateau/dip gives a measure to the pairing gap. The plateau and dip-like differential conductance spectra have been demonstrated in different 3D TI/superconductor heterostructures [115, 116]. For example, a Bi_2Se_3/$NbSe_2$ heterostructure device (Figure 8a) was fabricated by Li et al. [116] to study the superconductor proximity effect. The differential conductance spectra (Figure 8b) resolve a conductance plateau in the temperature range (4 K – 0.5 K) and a conductance peak develops at a temperature below 2 K. The origins of the conductance plateau and zero-bias peak are verified by their simulation results for the TI-SC junction with and without bulk conduction band involvement. The results suggest that both the surface and bulk states of the Bi_2Se_3 can participate in the superconducting proximity effect. The conductance plateau is solely due to the superconducting TSS, while the conductance peak is associated with the bulk states near the conduction band minimum. The width of the conductance plateau of ~2 meV at 0.5 K is comparable to the superconducting gap of $NbSe_2$ estimated from the BCS theory (~2.12 meV) [117], indicating a strong proximity effect. These results are consistent with spectroscopy studies in TI-SC heterostructures [39, 42, 118], suggesting the existence of a proximity induced topological superconductor (TSC), which is a precursor to the hosting of Majorana zero modes in the vortex core of the TSC. Despite several studies reporting zero bias conductance peaks by tunneling spectroscopy within the superconducting gap of the proximity induced TSC under small magnetic field [118, 119], the issue of distinguishing Majorana quasiparticle excitations from other low energy quasiparticle states is still a work in progress.

By constructing a lateral junction of two close-by superconductor electrodes separated by a 3D TI, the bound state of the Josephson effect can be studied. The Josephson junctions with 3D TIs can have bound supercurrents mediated by both the normal Andreev reflection and Majorana reflection mode. The Majorana bound state transfers only a single electron per cycle across the junction in contrast to the Copper pair transmission in Andreev reflection. They can be distinguished by the Shapiro response measurements in the Josephson junction. The transport of single electron via the Majorana reflection results in a suppression of odd Shapiro steps, manifesting a series of even Shapiro steps at a voltage sequence of $V= 2nV_0$ under a radio frequency excitation. The Shapiro voltage, V_0, is related to the excitation radio frequency as $V_0 = hf_{RF}/2e$. This intriguing skipped Shapiro step is referred to as the 4π-periodic energy phase dispersion [46-48]. This effect has been experimentally demonstrated by Schüffelgen et al. [120] in pseudo-four-terminal Shapiro measurements performed on an in situ fabricated Nb–$(Bi_{0.06}Sb_{0.94})_2Te_3$–Nb junctions (Figure 8c). As shown in Figure 8d, a fully suppressed first Shapiro dip was observed for excitation frequency of 3.0 GHz, in contrast to the full Shapiro step visible for 10 GHz and 7.8 GHz irradiations. The intriguing low excitation frequencies response in the BST Josephson junction can be explained by the small contribution of supercurrents from the Majorana bound state to the total supercurrent (as $I = I_{MBS} + I_{ABS}$), which directly affects the Majorana bound state frequency (as $f_{MBS} = I_{MBS}R_Ne/h$). Therefore, the suppression of the odd number of Shapiro steps becomes visible when f_{RF} is smaller than f_{MBS} [121].

Quantization of Majorana mode holds great promise for topological quantum computing. To realize the quantum effect, one can probe Majorana edge states by coupling a topologically nontrivial QH system to a superconducting reservoir [122, 123]. The Majorana edge state is topologically equivalent to a chiral topological superconductor with a topological number. However, QH edge states are impractical in 3D TI/superconductor as the required strong field (several teslas) to generate cyclotron motion in TSS, which can lead to the termination of the superconducting state. Compared to the QH system, the quantum anomalous Hall (QAH) insulator forms chiral edge modes without magnetic field (with the assistance of a small field to align the spin), which is more practical for realization the chiral topological superconductor. An important transport signature of the chiral Majorana edge states in the QAH insulator/superconductor heterostructure is the half-integer plateau in four-terminal conductance (σ_{12}) within the coercive field regime of the QAH insulator [124, 125]. In the bare QAH insulator, an applied external magnetic field can induce plateau transition between Chern number +/-1 and zero-plateau. In the QAH/superconductor hybrid system, the induced superconductivity in QAH can result in the additional Bogoliubov-de Gennes Chern number variation with half-integer conductance plateau developed near the zero-plateau transition. In a physical picture, this half-quantized plateau signifies an equal probability of backscattering between the normal and Andreev processes in the chiral Majorana edge state. Following the proposal by Wang et al. [124], the experimental observation was reported by He et al. [49] in a millimeter size Cr-doped $(Bi,Sb)_2Te_3$ QAH film with an Nb bar deposited in between two Hall channels (Figure 8e). As shown in Figure 8f, the developed half-integer conductance plateau near the QAH transition between full-integer and zero plateaus agrees well with the theoretical prediction. Nonetheless the origin of the half-quantized conductance plateau remains controversial. As suggested separately by Huang et al. [126] and Ji et al. [127], the percolation effect in a disordered QAH/superconductor junction or a good electrical contact effect between the QAH and the superconductor films can give rise to a similar effect.

7. Summary

In summary, we reviewed the transport properties of the 3D TIs and their related heterostructures with a focus on the exfoliated intrinsic 3D TIs from their bulk single crystals. The magnetotransport signatures which provide evidence of the TSS, namely the Landau quantization as manifested by quantum oscillations, QH plateaus, and quantum capacitance dips were discussed. The experimentally observed novel gapped surface states induced by intersurface hybridization, proximitized magnetic exchange coupling, and superconductivity pairing, which result in the intriguing topological phase transitions, quasi half-quantized Hall plateaus, and Majorana bound states, respectively, were also reviewed in the text. As a future outlook, the 3D TI based heterostructures fabricated in a clean manner, in particular through an atomically flat van der Waals platform, are expected to enhance the proximity coupling induced gapped states in 3D TIs, which will open opportunities to realize new topological phases in these heterostructures.

References

1. Hsieh, D., et al., *Observation of Unconventional Quantum Spin Textures in Topological Insulators.* Science, 2009. **323**(5916): p. 919-922.
2. Roushan, P., et al., *Topological surface states protected from backscattering by chiral spin texture.* Nature, 2009. **460**(7259): p. 1106-1109.
3. Chen, Y.L., et al., *Experimental Realization of a Three-Dimensional Topological Insulator, Bi<sub>2</sub>Te<sub>3</sub>.* Science, 2009. **325**(5937): p. 178.
4. Zhang, H., et al., *Topological insulators in Bi2Se3, Bi2Te3 and Sb2Te3 with a single Dirac cone on the surface.* Nature Physics, 2009. **5**(6): p. 438-442.
5. Bernevig, B.A., T.L. Hughes, and S.-C. Zhang, *Quantum Spin Hall Effect and Topological Phase Transition in HgTe Quantum Wells.* Science, 2006. **314**(5806): p. 1757.
6. Liu, C.-X., S.-C. Zhang, and X.-L. Qi, *The Quantum Anomalous Hall Effect: Theory and Experiment.* Annual Review of Condensed Matter Physics, 2016. **7**(1): p. 301-321.
7. Xu, S.-Y., et al., *Topological Phase Transition and Texture Inversion in a Tunable Topological Insulator.* Science, 2011. **332**(6029): p. 560.
8. Lian, B. and S.-C. Zhang, *Weyl semimetal and topological phase transition in five dimensions.* Physical Review B, 2017. **95**(23): p. 235106.
9. Rachel, S., *Interacting topological insulators: a review.* Reports on Progress in Physics, 2018. **81**(11): p. 116501.
10. Fu, L. and C.L. Kane, *Topological insulators with inversion symmetry.* Physical Review B, 2007. **76**(4): p. 045302.
11. Bernevig, B.A. and S.-C. Zhang, *Quantum Spin Hall Effect.* Physical Review Letters, 2006. **96**(10): p. 106802.

12. König, M., et al., *Quantum Spin Hall Insulator State in HgTe Quantum Wells.* Science, 2007. **318**(5851): p. 766.
13. Shen, S.-Q., *Topological Insulators: Dirac Equation in Condensed Matters.* 2012: Springer, Berlin, Heidelberg.
14. Shen, S.-Q., W.-Y. Shan, and H.-Z. Lu, *TOPOLOGICAL INSULATOR AND THE DIRAC EQUATION.* SPIN, 2011. **01**(01): p. 33-44.
15. Ando, T., T. Nakanishi, and R. Saito, *Berry's Phase and Absence of Back Scattering in Carbon Nanotubes.* Journal of the Physical Society of Japan, 1998. **67**(8): p. 2857-2862.
16. Mikitik, G.P. and Y.V. Sharlai, *Manifestation of Berry's Phase in Metal Physics.* Physical Review Letters, 1999. **82**(10): p. 2147-2150.
17. Chen, J., et al., *Gate-Voltage Control of Chemical Potential and Weak Antilocalization in ${\mathrm{Bi}}_{2}{\mathrm{Se}}_{3}$.* Physical Review Letters, 2010. **105**(17): p. 176602.
18. Checkelsky, J.G., et al., *Bulk Band Gap and Surface State Conduction Observed in Voltage-Tuned Crystals of the Topological Insulator ${\mathrm{Bi}}_{2}{\mathrm{Se}}_{3}$.* Physical Review Letters, 2011. **106**(19): p. 196801.
19. Xu, Y., et al., *Observation of topological surface state quantum Hall effect in an intrinsic three-dimensional topological insulator.* Nat Phys, 2014. **10**(12): p. 956-963.
20. Yoshimi, R., et al., *Quantum Hall effect on top and bottom surface states of topological insulator (Bi1−xSbx)2Te3 films.* Nature Communications, 2015. **6**(1): p. 6627.
21. Ando, Y., *Topological Insulator Materials.* Journal of the Physical Society of Japan, 2013. **82**(10): p. 102001.
22. Fu, L. and C.L. Kane, *Superconducting Proximity Effect and Majorana Fermions at the Surface of a Topological Insulator.* Physical Review Letters, 2008. **100**(9): p. 096407.
23. Hor, Y.S., et al., *Superconductivity in ${\mathrm{Cu}}_{x}{\mathrm{Bi}}_{2}{\mathrm{Se}}_{3}$ and its Implications for Pairing in the Undoped Topological Insulator.* Physical Review Letters, 2010. **104**(5): p. 057001.
24. Li, C.H., et al., *Electrical detection of charge-current-induced spin polarization due to spin-momentum locking in Bi2Se3.* Nature Nanotechnology, 2014. **9**(3): p. 218-224.
25. Liu, H., et al., *Dephasing Effect on Backscattering of Helical Surface States in 3D Topological Insulators.* Physical Review Letters, 2014. **113**(4): p. 046805.
26. Zhou, Y.-F., et al., *Two-dimensional lattice model for the surface states of topological insulators.* Physical Review B, 2017. **95**(24): p. 245137.
27. Liu, C.-X., et al., *Model Hamiltonian for topological insulators.* Physical Review B, 2010. **82**(4): p. 045122.
28. Checkelsky, J.G., et al., *Quantum Interference in Macroscopic Crystals of Nonmetallic ${\mathrm{Bi}}_{2}{\mathrm{Se}}_{3}$.* Physical Review Letters, 2009. **103**(24): p. 246601.
29. Men'shov, V.N., et al., *Magnetic proximity effect in the three-dimensional topological insulator/ferromagnetic insulator heterostructure.* Physical Review B, 2013. **88**(22): p. 224401.
30. Jiang, Y., et al., *Mass acquisition of Dirac fermions in magnetically doped topological insulator $\mathrm{S}{\mathrm{b}}_{2}\mathrm{T}{\mathrm{e}}_{3}$ films.* Physical Review B, 2015. **92**(19): p. 195418.

31. Yang, S.R., et al., *Evidence for exchange Dirac gap in magnetotransport of topological insulator--magnetic insulator heterostructures.* Physical Review B, 2019. **100**(4): p. 045138.
32. Hirahara, T., et al., *Large-Gap Magnetic Topological Heterostructure Formed by Subsurface Incorporation of a Ferromagnetic Layer.* Nano Letters, 2017. **17**(6): p. 3493-3500.
33. Alegria, L.D., et al., *Large anomalous Hall effect in ferromagnetic insulator-topological insulator heterostructures.* Applied Physics Letters, 2014. **105**(5): p. 053512.
34. Liu, N., J. Teng, and Y. Li, *Two-component anomalous Hall effect in a magnetically doped topological insulator.* Nature Communications, 2018. **9**(1): p. 1282.
35. Lu, H.-Z., J. Shi, and S.-Q. Shen, *Competition between Weak Localization and Antilocalization in Topological Surface States.* Physical Review Letters, 2011. **107**(7): p. 076801.
36. Zhang, S., et al., *Anomalous quantization trajectory and parity anomaly in Co cluster decorated BiSbTeSe2 nanodevices.* Nature Communications, 2017. **8**(1): p. 977.
37. Stanescu, T.D., et al., *Proximity effect at the superconductor--topological insulator interface.* Physical Review B, 2010. **81**(24): p. 241310.
38. Zhang, Y.-T., et al., *High-Efficiency Cooper-Pair Splitter in Quantum Anomalous Hall Insulator Proximity-Coupled with Superconductor.* Scientific Reports, 2015. **5**(1): p. 14892.
39. Trang, C.X., et al., *Conversion of a conventional superconductor into a topological superconductor by topological proximity effect.* Nature Communications, 2020. **11**(1): p. 159.
40. Bhattacharyya, B., et al., *Proximity-induced supercurrent through topological insulator based nanowires for quantum computation studies.* Scientific Reports, 2018. **8**(1): p. 17237.
41. Qi, X.-L. and S.-C. Zhang, *Topological insulators and superconductors.* Reviews of Modern Physics, 2011. **83**(4): p. 1057-1110.
42. Wang, M.-X., et al., *The Coexistence of Superconductivity and Topological Order in the Bi<sub>2</sub>Se<sub>3</sub> Thin Films.* Science, 2012. **336**(6077): p. 52.
43. Fu, L. and C.L. Kane, *Josephson current and noise at a superconductor/quantum-spin-Hall-insulator/superconductor junction.* Physical Review B, 2009. **79**(16): p. 161408.
44. Nichele, F., et al., *Scaling of Majorana Zero-Bias Conductance Peaks.* Physical Review Letters, 2017. **119**(13): p. 136803.
45. Lutchyn, R.M., et al., *Majorana zero modes in superconductor–semiconductor heterostructures.* Nature Reviews Materials, 2018. **3**(5): p. 52-68.
46. van Heck, B., et al., *Coulomb stability of the 4$\ensuremath{\pi}$-periodic Josephson effect of Majorana fermions.* Physical Review B, 2011. **84**(18): p. 180502.
47. Bocquillon, E., et al., *Gapless Andreev bound states in the quantum spin Hall insulator HgTe.* Nature Nanotechnology, 2017. **12**(2): p. 137-143.
48. Veldhorst, M., et al., *Josephson supercurrent through a topological insulator surface state.* Nature Materials, 2012. **11**(5): p. 417-421.
49. He, Q.L., et al., *Chiral Majorana fermion modes in a quantum anomalous Hall insulator–superconductor structure.* Science, 2017. **357**(6348): p. 294.

50. Xia, Y., et al., *Observation of a large-gap topological-insulator class with a single Dirac cone on the surface.* Nature Physics, 2009. **5**(6): p. 398-402.
51. Peng, H., et al., *Aharonov–Bohm interference in topological insulator nanoribbons.* Nature Materials, 2010. **9**(3): p. 225-229.
52. Xiu, F., et al., *Manipulating surface states in topological insulator nanoribbons.* Nature Nanotechnology, 2011. **6**(4): p. 216-221.
53. Cho, S., et al., *Aharonov–Bohm oscillations in a quasi-ballistic three-dimensional topological insulator nanowire.* Nature Communications, 2015. **6**(1): p. 7634.
54. Cho, S., et al., *Topological Insulator Quantum Dot with Tunable Barriers.* Nano Letters, 2012. **12**(1): p. 469-472.
55. Lu, X., et al., *Nanoimaging of Electronic Heterogeneity in Bi2Se3 and Sb2Te3 Nanocrystals.* Advanced Electronic Materials, 2018. **4**(1): p. 1700377.
56. Koirala, N., et al., *Record Surface State Mobility and Quantum Hall Effect in Topological Insulator Thin Films via Interface Engineering.* Nano Letters, 2015. **15**(12): p. 8245-8249.
57. Salehi, M., et al., *Quantum-Hall to Insulator Transition in Ultra-Low-Carrier-Density Topological Insulator Films and a Hidden Phase of the Zeroth Landau Level.* Advanced Materials, 2019. **31**(36): p. 1901091.
58. Telford, E.J., et al., *Via Method for Lithography Free Contact and Preservation of 2D Materials.* Nano Letters, 2018. **18**(2): p. 1416-1420.
59. Pizzocchero, F., et al., *The hot pick-up technique for batch assembly of van der Waals heterostructures.* Nature Communications, 2016. **7**(1): p. 11894.
60. Yang, S.-J., et al., *All-Dry Transfer of Graphene Film by van der Waals Interactions.* Nano Letters, 2019. **19**(6): p. 3590-3596.
61. Han, K.-B., et al., *Enhancement in surface mobility and quantum transport of Bi2−xSbxTe3−ySey topological insulator by controlling the crystal growth conditions.* Scientific Reports, 2018. **8**(1): p. 17290.
62. Ali, M.N., et al., *Correlation of crystal quality and extreme magnetoresistance of WTe 2.* EPL (Europhysics Letters), 2015. **110**(6): p. 67002.
63. Kim, D., et al., *Surface conduction of topological Dirac electrons in bulk insulating Bi2Se3.* Nature Physics, 2012. **8**(6): p. 459-463.
64. Shoenberg, D., *Magnetic Oscillations in Metals*. Cambridge Monographs on Physics. 1984, Cambridge: Cambridge University Press.
65. Qu, D.-X., et al., *Quantum Oscillations and Hall Anomaly of Surface States in the Topological Insulator Bi<sub>2</sub>Te<sub>3</sub>.* Science, 2010. **329**(5993): p. 821.
66. Taskin, A.A., et al., *Observation of Dirac Holes and Electrons in a Topological Insulator.* Physical Review Letters, 2011. **107**(1): p. 016801.
67. Xu, Y., I. Miotkowski, and Y.P. Chen, *Quantum transport of two-species Dirac fermions in dual-gated three-dimensional topological insulators.* Nature Communications, 2016. **7**(1): p. 11434.
68. Zhang, Y., et al., *Experimental observation of the quantum Hall effect and Berry's phase in graphene.* Nature, 2005. **438**(7065): p. 201-204.
69. Analytis, J.G., et al., *Two-dimensional surface state in the quantum limit of a topological insulator.* Nature Physics, 2010. **6**(12): p. 960-964.

70. Yu, G.L., et al., *Interaction phenomena in graphene seen through quantum capacitance.* Proceedings of the National Academy of Sciences, 2013. **110**(9): p. 3282.
71. Martin, J., et al., *Local Compressibility Measurements of Correlated States in Suspended Bilayer Graphene.* Physical Review Letters, 2010. **105**(25): p. 256806.
72. Young, A.F., et al., *Electronic compressibility of layer-polarized bilayer graphene.* Physical Review B, 2012. **85**(23): p. 235458.
73. Henriksen, E.A. and J.P. Eisenstein, *Measurement of the electronic compressibility of bilayer graphene.* Physical Review B, 2010. **82**(4): p. 041412.
74. Chong, S.K., et al., *Landau Levels of Topologically-Protected Surface States Probed by Dual-Gated Quantum Capacitance.* ACS Nano, 2020. **14**(1): p. 1158-1165.
75. Tilahun, D., et al., *Quantum Hall Superfluids in Topological Insulator Thin Films.* Physical Review Letters, 2011. **107**(24): p. 246401.
76. Seradjeh, B., J.E. Moore, and M. Franz, *Exciton Condensation and Charge Fractionalization in a Topological Insulator Film.* Physical Review Letters, 2009. **103**(6): p. 066402.
77. Kim, Y., E.M. Hankiewicz, and M.J. Gilbert, *Topological excitonic superfluids in three dimensions.* Physical Review B, 2012. **86**(18): p. 184504.
78. Chong, S.K., et al., *Tunable Coupling between Surface States of a Three-Dimensional Topological Insulator in the Quantum Hall Regime.* Physical Review Letters, 2019. **123**(3): p. 036804.
79. Zyuzin, A.A. and A.A. Burkov, *Thin topological insulator film in a perpendicular magnetic field.* Physical Review B, 2011. **83**(19): p. 195413.
80. Tahir, M., K. Sabeeh, and U. Schwingenschlögl, *Quantum magnetotransport properties of ultrathin topological insulator films.* Journal of Applied Physics, 2013. **113**(4): p. 043720.
81. Pertsova, A., C.M. Canali, and A.H. MacDonald, *Thin films of a three-dimensional topological insulator in a strong magnetic field: Microscopic study.* Physical Review B, 2015. **91**(7): p. 075430.
82. Yang, Z. and J.H. Han, *Landau level states on a topological insulator thin film.* Physical Review B, 2011. **83**(4): p. 045415.
83. Du, L., et al., *Evidence for a topological excitonic insulator in InAs/GaSb bilayers.* Nature Communications, 2017. **8**(1): p. 1971.
84. Zhang, Y., et al., *Crossover of the three-dimensional topological insulator Bi2Se3 to the two-dimensional limit.* Nature Physics, 2010. **6**(8): p. 584-588.
85. Kim, D., et al., *Coherent topological transport on the surface of Bi2Se3.* Nature Communications, 2013. **4**(1): p. 2040.
86. Hai-Zhou, L. and S. Shun-Qing. *Weak localization and weak anti-localization in topological insulators*. in *Proc.SPIE*. 2014.
87. Liu, M., et al., *Crossover between Weak Antilocalization and Weak Localization in a Magnetically Doped Topological Insulator.* Physical Review Letters, 2012. **108**(3): p. 036805.
88. Taskin, A.A., et al., *Manifestation of Topological Protection in Transport Properties of Epitaxial ${\mathrm{Bi}}_{2}{\mathrm{Se}}_{3}$ Thin Films.* Physical Review Letters, 2012. **109**(6): p. 066803.
89. Cho, S., et al., *Insulating Behavior in Ultrathin Bismuth Selenide Field Effect Transistors.* Nano Letters, 2011. **11**(5): p. 1925-1927.

90. Zyuzin, A.A., M.D. Hook, and A.A. Burkov, *Parallel magnetic field driven quantum phase transition in a thin topological insulator film.* Physical Review B, 2011. **83**(24): p. 245428.
91. Xu, Y., et al., *Tuning Insulator-Semimetal Transitions in 3D Topological Insulator thin Films by Intersurface Hybridization and In-Plane Magnetic Fields.* Physical Review Letters, 2019. **123**(20): p. 207701.
92. Kim, M., et al., *Topological quantum phase transitions driven by external electric fields in Sb<sub>2</sub>Te<sub>3</sub> thin films.* Proceedings of the National Academy of Sciences, 2012. **109**(3): p. 671.
93. Li, J. and K. Chang, *Electric field driven quantum phase transition between band insulator and topological insulator.* Applied Physics Letters, 2009. **95**(22): p. 222110.
94. Wang, J., B. Lian, and S.-C. Zhang, *Electrically Tunable Magnetism in Magnetic Topological Insulators.* Physical Review Letters, 2015. **115**(3): p. 036805.
95. Zhang, T., et al., *Electric-Field Tuning of the Surface Band Structure of Topological Insulator ${\mathrm{Sb}}_{2}{\mathrm{Te}}_{3}$ Thin Films.* Physical Review Letters, 2013. **111**(5): p. 056803.
96. Chong, S.K., Liu, L., Sparks, T. D., Liu, F. and Deshpande, V. V., *Topological Phase Transitions in a Hybridized Three-Dimensional Topological Insulator*. 2020, cond-mat.mes-hall: arXiv.
97. Khang, N.H.D., Y. Ueda, and P.N. Hai, *A conductive topological insulator with large spin Hall effect for ultralow power spin–orbit torque switching.* Nature Materials, 2018. **17**(9): p. 808-813.
98. Fan, Y., et al., *Electric-field control of spin–orbit torque in a magnetically doped topological insulator.* Nature Nanotechnology, 2016. **11**(4): p. 352-359.
99. Han, J., et al., *Room-Temperature Spin-Orbit Torque Switching Induced by a Topological Insulator.* Physical Review Letters, 2017. **119**(7): p. 077702.
100. Wang K.L., L.M., Kou X. , *Spintronics of Topological Insulators*. Handbook of Spintronics, ed. A.D. Xu Y., Nitta J. 2016, Dordrecht: Springer.
101. Fan, Y. and K.L. Wang, *Spintronics Based on Topological Insulators.* SPIN, 2016. **06**(02): p. 1640001.
102. Samarth, N. *Topological spintronics*. in *2016 Compound Semiconductor Week (CSW) [Includes 28th International Conference on Indium Phosphide & Related Materials (IPRM) & 43rd International Symposium on Compound Semiconductors (ISCS)*. 2016.
103. Khmelnitskii, D.E., *Quantization of Hall conductivity.* Jetp Lett., 1983. **38**: p. 552–556.
104. Chong, S.K., et al., *Topological Insulator-Based van der Waals Heterostructures for Effective Control of Massless and Massive Dirac Fermions.* Nano Letters, 2018. **18**(12): p. 8047-8053.
105. Semenoff, G.W., *Condensed-Matter Simulation of a Three-Dimensional Anomaly.* Physical Review Letters, 1984. **53**(26): p. 2449-2452.
106. Redlich, A.N., *Gauge Noninvariance and Parity Nonconservation of Three-Dimensional Fermions.* Physical Review Letters, 1984. **52**(1): p. 18-21.
107. Lapa, M.F., *Parity anomaly from the Hamiltonian point of view.* Physical Review B, 2019. **99**(23): p. 235144.
108. Qi, X.-L., T.L. Hughes, and S.-C. Zhang, *Topological field theory of time-reversal invariant insulators.* Physical Review B, 2008. **78**(19): p. 195424.

109. Wang, J., et al., *Quantized topological magnetoelectric effect of the zero-plateau quantum anomalous Hall state.* Physical Review B, 2015. **92**(8): p. 081107.
110. Moore, J.E. and L. Balents, *Topological invariants of time-reversal-invariant band structures.* Physical Review B, 2007. **75**(12): p. 121306.
111. Sato, M. and S. Fujimoto, *Majorana Fermions and Topology in Superconductors.* Journal of the Physical Society of Japan, 2016. **85**(7): p. 072001.
112. Lian, B., et al., *Topological quantum computation based on chiral Majorana fermions.* Proceedings of the National Academy of Sciences, 2018. **115**(43): p. 10938.
113. Blonder, G.E., M. Tinkham, and T.M. Klapwijk, *Transition from metallic to tunneling regimes in superconducting microconstrictions: Excess current, charge imbalance, and supercurrent conversion.* Physical Review B, 1982. **25**(7): p. 4515-4532.
114. Knoch, J., J. Appenzeller, and B. Lengeler, *Preparation of highly transparent superconductor-semiconductor contacts.* Journal of Applied Physics, 2000. **88**(6): p. 3522-3526.
115. Banerjee, A., et al., *Signatures of Topological Superconductivity in Bulk-Insulating Topological Insulator BiSbTe1.25Se1.75 in Proximity with Superconducting NbSe2.* ACS Nano, 2018. **12**(12): p. 12665-12672.
116. Li, H., et al., *Origin of bias-independent conductance plateaus and zero-bias conductance peaks in ${\mathrm{Bi}}_{2}{\mathrm{Se}}_{3}/{\mathrm{NbSe}}_{2}$ hybrid structures.* Physical Review B, 2017. **96**(7): p. 075107.
117. Clayman, B.P. and R.F. Frindt, *The superconducting energy gap of NbSe2.* Solid State Communications, 1971. **9**(22): p. 1881-1884.
118. Xu, J.-P., et al., *Experimental Detection of a Majorana Mode in the core of a Magnetic Vortex inside a Topological Insulator-Superconductor ${\mathrm{Bi}}_{2}{\mathrm{Te}}_{3}/{\mathrm{NbSe}}_{2}$ Heterostructure.* Physical Review Letters, 2015. **114**(1): p. 017001.
119. Sun, H.-H., et al., *Majorana Zero Mode Detected with Spin Selective Andreev Reflection in the Vortex of a Topological Superconductor.* Physical Review Letters, 2016. **116**(25): p. 257003.
120. Schüffelgen, P., et al., *Selective area growth and stencil lithography for in situ fabricated quantum devices.* Nature Nanotechnology, 2019. **14**(9): p. 825-831.
121. Wiedenmann, J., et al., *4π-periodic Josephson supercurrent in HgTe-based topological Josephson junctions.* Nature Communications, 2016. **7**(1): p. 10303.
122. Peralta Gavensky, L., G. Usaj, and C.A. Balseiro, *Majorana fermions on the quantum Hall edge.* Physical Review Research, 2020. **2**(3): p. 033218.
123. Read, N. and D. Green, *Paired states of fermions in two dimensions with breaking of parity and time-reversal symmetries and the fractional quantum Hall effect.* Physical Review B, 2000. **61**(15): p. 10267-10297.
124. Wang, J., et al., *Chiral topological superconductor and half-integer conductance plateau from quantum anomalous Hall plateau transition.* Physical Review B, 2015. **92**(6): p. 064520.
125. Yan, Q., Y.-F. Zhou, and Q.-F. Sun, *Electrically tunable chiral Majorana edge modes in quantum anomalous Hall insulator--topological superconductor systems.* Physical Review B, 2019. **100**(23): p. 235407.

126. Huang, Y., F. Setiawan, and J.D. Sau, *Disorder-induced half-integer quantized conductance plateau in quantum anomalous Hall insulator-superconductor structures.* Physical Review B, 2018. **97**(10): p. 100501.
127. Ji, W. and X.-G. Wen, *$\frac{1}{2}({e}^{2}/h)$ Conductance Plateau without 1D Chiral Majorana Fermions.* Physical Review Letters, 2018. **120**(10): p. 107002.

Acknowledgements

This material is based upon work supported by the National Science Foundation the Quantum Leap Big Idea under Grant No. 1936383.

Figures

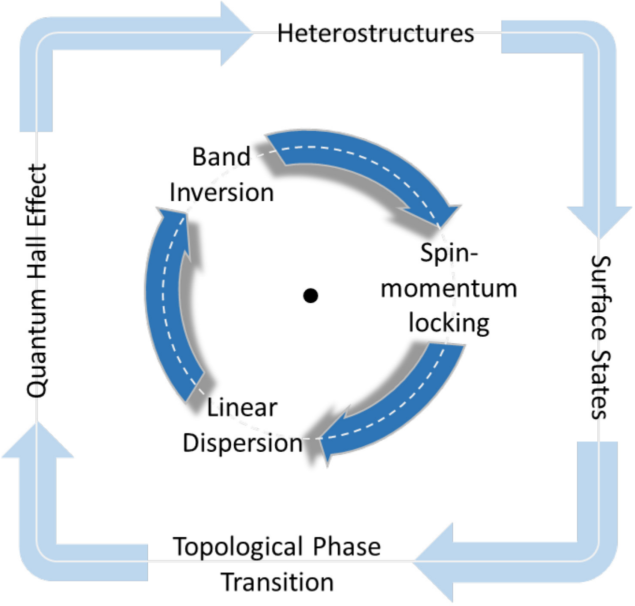

Figure 1. Overview. Intrinsic characteristics and central research topics of three-dimensional topological insulators. The inverted bulk gap in 3D TIs is an essential requirement to host topological surface states. The topological surface states are characterized by a linear energy dispersion with a helical spin texture. A consequence of the topological surface states is the manifestation of the half-integer quantum Hall effect. Interfacing 3D TIs with magnetic or superconducting layers can break the time-reversal symmetry and gives rise to non-trivial surface gap states. Manipulation of the surface gap's topology is key to realize the topological quantum phase transition.

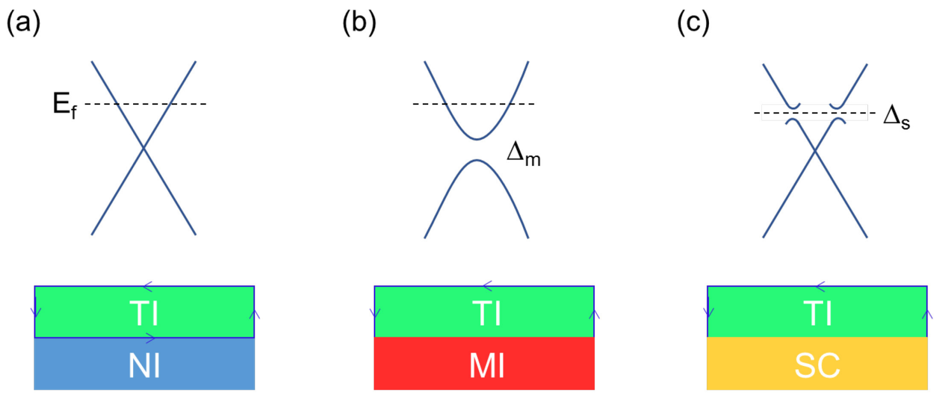

Figure 2. 3D TI-based heterostructures. (bottom) Heterostructures of 3D TI film with (a) normal insulator, (b) magnetic layer, and (c) superconductor. The blue arrow lines represent the topological surface states. (top) Their corresponding band structures at the heterostructure interface. (a) Gapless topological surface state, (b) and (c) gapped TSS with proximity-induced exchange (Δ_m) and pairing (Δ_s) gaps, respectively. The black dashed lines indicate the Fermi level of the 3D TI.

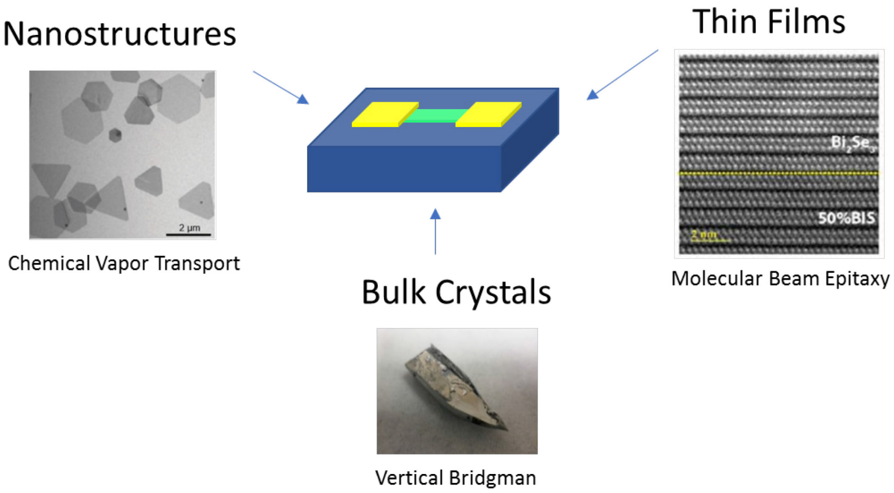

Figure 3. Synthetic routes. An illustration of a 3D TI device fabricated from the raw materials grown by different synthesis methods. (left) TEM micrograph of TI nanocrystals grown by chemical vapor transport. Adapted from Ref. [55] (right) Cross-sectional HRTEM of a TI thin films grown by a molecular beam epitaxy. Adapted from Ref. [56] (bottom) TI bulk crystal grown by a vertical Bridgman furnace served as parent material for random exfoliation into thin flakes. Adapted from Ref. [61]

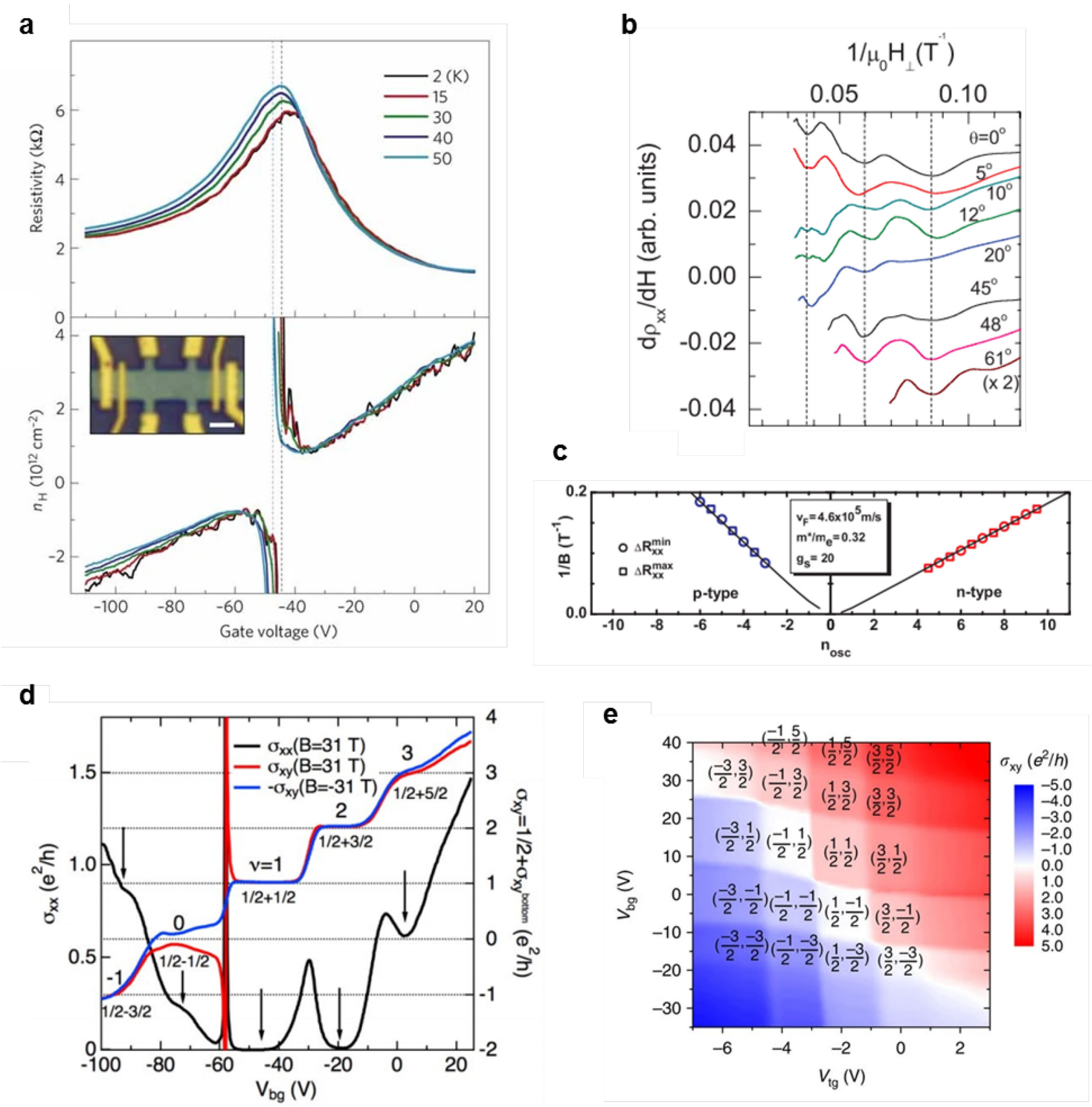

Figure 4. Topological surface states. (a) The top panel shows the resistivity of an exfoliated 10 nm Bi_2Se_3 thin flake (device shown in the inset) as a function of V_g measured at different temperatures. The bottom panel shows the carrier density calculated from ρ_H as a function of V_g. The linear dependence of carrier density with V_g indicates the ambipolar transport by gate tuning. Adapted from Ref. [63] (b) $d\rho_{xx}/dH$ as a function of a magnetic field for a Bi_2Te_3 bulk crystal with a variation of tilt angle between the surface normal and magnetic field. Vertical dashed lines trace the minima corresponding to LLs for the different curves. Adapted from Ref. [65] (c) LL fan plots of magnetic field versus LL indices extracted from the R_{xx} maxima and minima in a 30 μm thick $Bi_{1.5}Sb_{0.5}Te_{1.7}Se_{1.3}$ flake. The blue (left) and red (right) data points are measured from the same sample at its fresh and aged conditions, respectively, and its chemical potential shifted naturally from p-type to n-type. The solid lines are fitting to the SdH oscillations. Adapted from Ref. [66] (d) Quantum Hall effect (QHE) of the TSS observed at a high magnetic field of 31 T in an exfoliated 160 nm $BiSbTeSe_2$ flake. The arrows point to the σ_{xx} minima corresponding to the quantum Hall plateau in σ_{xy}. Adapted from Ref. [19] (e) Color map of σ_{xy} as functions of V_{bg} and V_{tg} measured at a magnetic field of 18T. The LL filling factors of the top and bottom topological surface states are indexed in the map as (ν_t,ν_b). Adapted from Ref. [67]

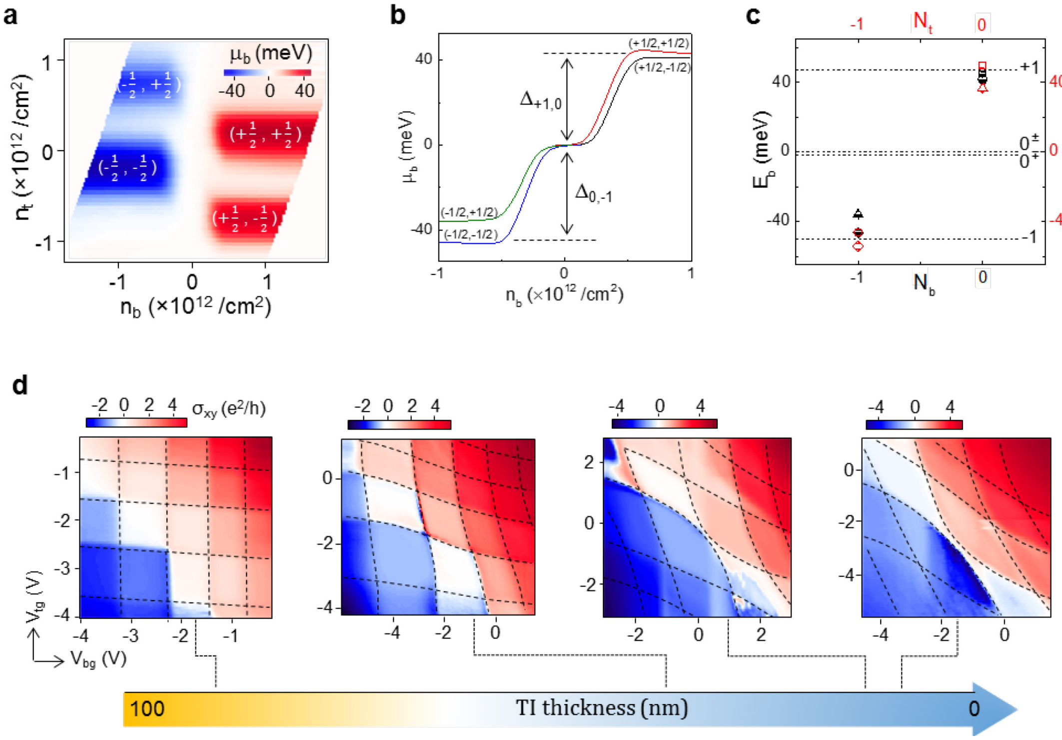

Figure 5. Capacitive-coupling in QHE. (a) 2D color map of the chemical potential of bottom surface state (μ_b) as a function of charge density of top (n_t) and bottom (n_b) surfaces as derived from the quantum capacitance of a 17 nm thin $BiSbTeSe_2$ device. Labels in (a) are the filled LL filling factors in the bottom and top surfaces (ν_b, ν_t). (b) Line cuts of $\mu_b(n_b)$ curves at different QH plateaus of (ν_b, ν_t) as indexed in the figure. The LL energy spacings are derived from the step heights of the $\mu_b(n_b)$ curves as labeled in the figure. (c) The LL energies of the bottom surface, E_b (black dots), and top surface, E_t (red dots), for the corresponding LL indices, N_b and N_t. The notations of $0^\pm$ and $0^\mp$ are used for (ν_b, ν_t) of (+½,-½) and (-½,+½), respectively, to distinguish the two $\nu = 0$ QH states. Adapted from Ref. [74] (d) Color maps of σ_{xy} as functions of dual gate voltages for the 89 nm, 31 nm, 16 nm, and 10 nm $BiSbTeSe_2$ devices measured at a magnetic field of 18 T. The dashed lines in the maps trace the boundaries of LL indices N_t and N_b for top and bottom surfaces. The colors in the arrow scale (bottom) indicate the thickness of TI flake with (blue) and without (yellow) capacitive-coupling. Adapted from Ref. [78]

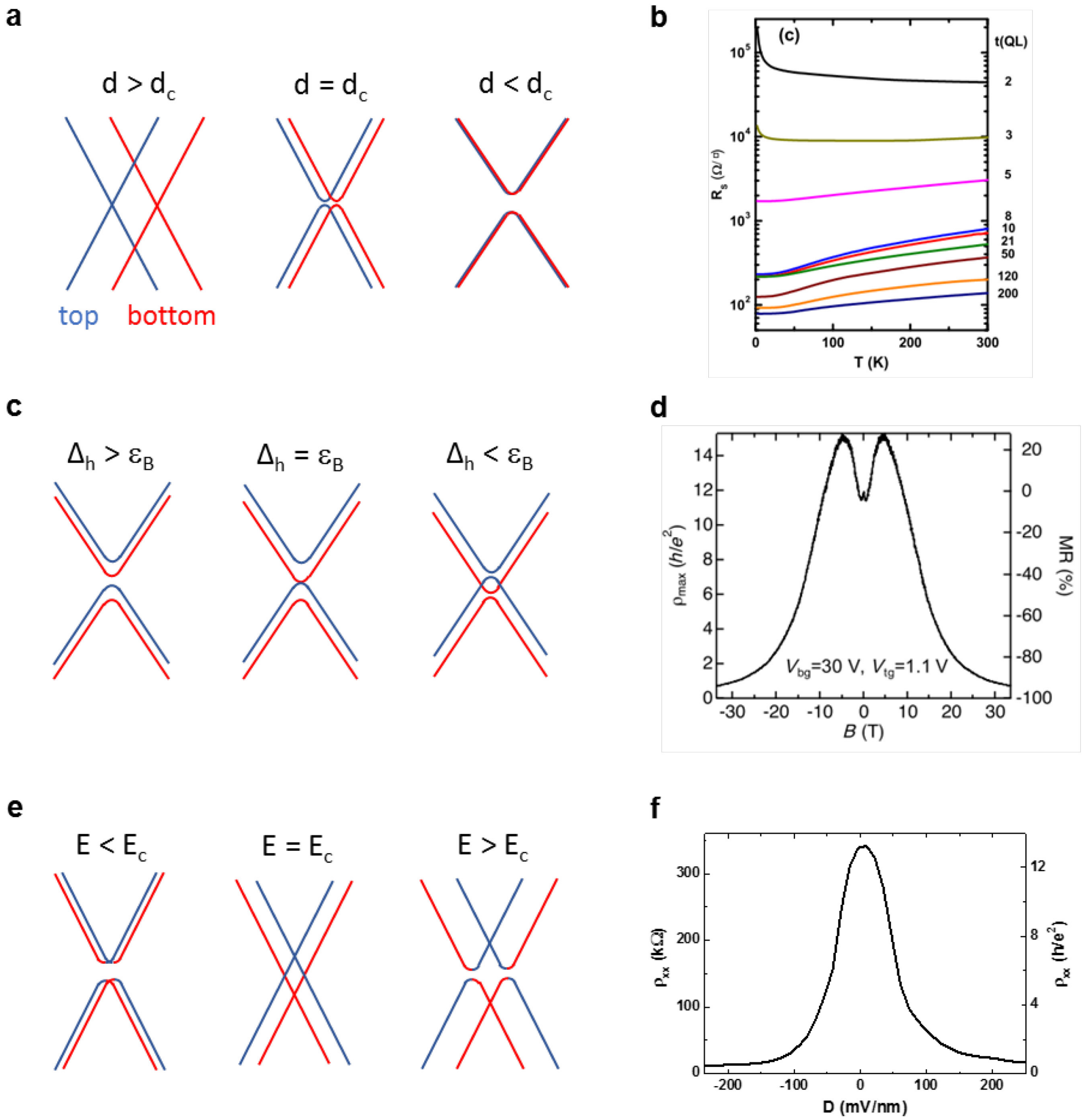

Figure 6. Topological phase transitions. Schematic of surface band structures at different (a) thickness, (c) in-plane magnetic field, and (e) electric field for illustration of topological phase transition at 2D crossover regime of a 3D topological insulator. (b) Temperature-dependent sheet resistance for Bi_2Se_3 thin films with different thickness from 200 nm down to 2 nm. Adapted from Ref. [88] (d) Maximum resistivity and magnetoresistance as a function of the in-plane magnetic field of a 10 nm $BiSbTeSe_2$ flake. Adapted from Ref. [91] (f) Longitudinal resistance as a function of displacement field of a 9 nm $BiSbTeSe_2$ flake. Adapted from Ref. [96]

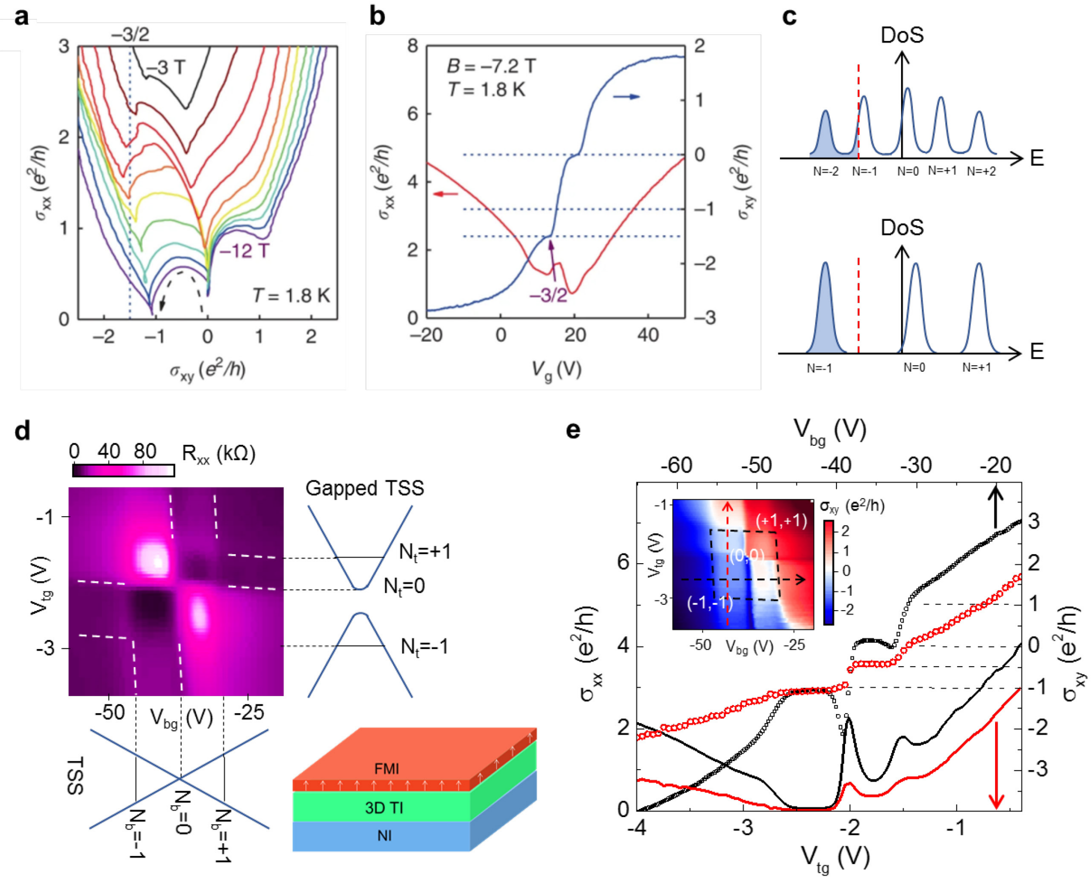

Figure 7. TI/ferromagnet heterostructures. RGF diagram analysis in (a) σ_{xx} versus σ_{xy} plane, and (b) σ_{xx} (σ_{xy}) versus gate voltage (V_g) plots for a Co-particles decorated $BiSbTeSe_2$ device. The vertical dashed line in (a) and tilted arrow in (b) indicate the -3/2 QH plateau observed at -7 T and 1.8 K. (c) Schematic of the density of states of TSS at low (top) and high (bottom) magnetic fields for the illustration of the delayed LL hybridization model of the top surface with Co-decoration. Adapted from Ref. [36] (d) Color map of R_{xx} as a function of V_{tg} and V_{bg} at a magnetic field of 9 T for a $BiSbTeSe_2$/$CrGeTe_3$/graphite device as illustrated in the drawing in (d). Schematic of the LL band diagrams of the top gapped and bottom gapless TSS extended from the R_{xx} maps. (e) σ_{xx} (σ_{xy}) versus V_{tg} and V_{bg} plots extracted from the red (black) line profiles in the σ_{xy} versus dualgate color map measured at a magnetic field of 9 T. Inset in (e) is the map of the σ_{xy} of the $BiSbTeSe_2$ as the function of dual-gate voltages. The black and red arrow lines represent the V_{tg} and V_{bg} where the line profiles in (e) were obtained. The (N_t, N_b) are indexed in the color map. Adapted from Ref. [104]

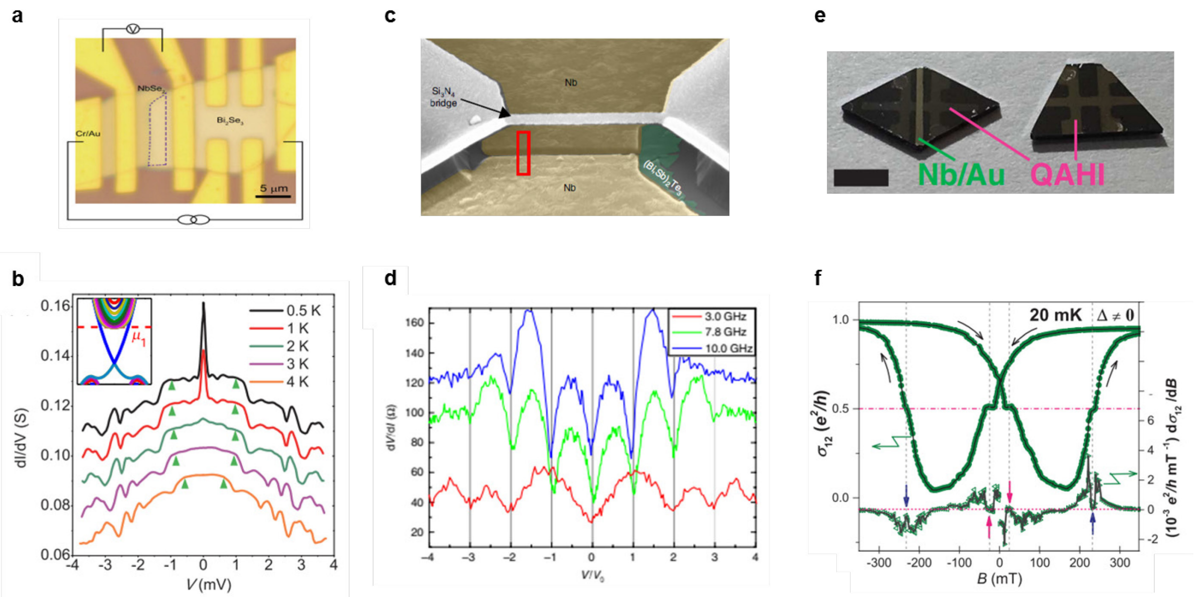

Figure 8. TI/superconductor heterostructures. (a) $Bi_2Se_3/NbSe_2$ heterostructure device for probing the proximity induced superconducting gap. (b) differential conductance (dI/dV) as a function of bias voltage for the device in (a) measured at different temperatures. (Inset) Simulated band structure of the TI/SC junction with Fermi level located slightly above the bulk conduction band edge. Adapted from Ref. [116] (c) False-color SEM micrograph of an in situ fabricated $(Bi,Sb)_2Te_3$/Nb Josephson junction. The stencil bridge casts a shadow that divides the Nb thin film into two electrodes with separation ~100 nm, which are solely interconnected by the $(Bi_{0.06}Sb_{0.94})_2Te_3$ weak link. (d) Voltage dependency of Shapiro response dV/dI of the device in (c) measured at three different f_{RF} of 3.0, 7.8 and 10.0 GHz excitations at $T = 1.5$ K. Adapted from Ref. [120] (e) Hard mask fabricated Cr-doped BST with (left) and without (right) Nb bar grown on GaAs substrate. (f) Conductivity σ_{12} (left) and the derivation $d\sigma_{12}/dB$ (right) versus magnetic field for the Nb/CBST heterojunction device in (e) measured at 20 mK. Adapted from Ref. [49]